

# A Threshold Gas Čerenkov Detector for the Spin Asymmetries of the Nucleon Experiment

Whitney R. Armstrong<sup>a,\*</sup>, Seonho Choi<sup>b</sup>, Ed Kaczanowicz<sup>a</sup>, Alexander Lukhanin<sup>a</sup>, Zein-Eddine Meziani<sup>a</sup>, Brad Sawatzky<sup>a,c</sup>

<sup>a</sup>*Department of Physics, Temple University, Philadelphia, PA, 19122, USA*

<sup>b</sup>*Seoul National University, Seoul 151-747, Korea*

<sup>c</sup>*Thomas Jefferson National Accelerator Facility, Newport News, Va, 23606, USA*

---

## Abstract

We report on the design, construction, commissioning, and performance of a threshold gas Čerenkov counter in an open configuration, which operates in a high luminosity environment and produces a high photo-electron yield. Part of a unique open geometry detector package known as the Big Electron Telescope Array, this Čerenkov counter served to identify scattered electrons and reject produced pions in an inclusive scattering experiment known as the Spin Asymmetries of the Nucleon Experiment E07-003 at the Thomas Jefferson National Accelerator Facility (TJNAF) also known as Jefferson Lab. The experiment consisted of a measurement of double spin asymmetries  $A_{\parallel}$  and  $A_{\perp}$  of a polarized electron beam impinging on a polarized ammonia target. The Čerenkov counter's performance is characterised by a yield of about 20 photoelectrons per electron or positron track. Thanks to this large number of photoelectrons per track, the Čerenkov counter had enough resolution to identify electron-positron pairs from the conversion of photons resulting mainly from  $\pi^0$  decays.

*Keywords:* Threshold Gas Čerenkov Detector, SANE, Particle Identification  
*PACS:* 29.40.Ka

---

## 1. Introduction

Čerenkov counters have been used in high energy electron scattering experiments as part of detector stacks within shielded spectrometers, especially at low duty cycle beam facilities where the instantaneous beam current was at the milliamp level. With the advent of continuous electron beams with very high duty cycle it became feasible to use Čerenkov counters in an open environment for the same average beam current. In the SANE experiment data were collected in Hall C at Jefferson Lab using a threshold gas Čerenkov counter, as an

---

\*Corresponding author

*Email address:* whit@temple.edu (Whitney R. Armstrong)

integral part of a new detector package known as the Big Electron Telescope Array (BETA), which identified scattered electrons, measured their scattered angle and their energy. BETA, shown in figure 1, consisted of a forward tracker, a gas Čerenkov detector which is the focus of this report, a Lucite hodoscope and a lead-glass calorimeter.

Using a polarized electron beam and a polarized ammonia target, The SANE collaboration [1] set out to measure two observables, known as double spin asymmetries,  $A_{\parallel}$  and  $A_{\perp}$ . These are measured with two different configurations, parallel or perpendicular, of the spin directions of the beam and the target. The electron beam’s helicity was flipped while the spin direction of the target has been fixed. To detect the scattered electrons BETA was positioned at a central scattering angle of 40 degrees, covering roughly  $\pm 5^{\circ}$  in scattering angle, and from about 700 MeV up to about 2.5 GeV in energy, thus covering a kinematic range of Bjorken  $x$  and four momentum transfer  $Q^2$  corresponding to  $0.3 < x < 0.8$  and  $2.5 \text{ GeV}^2 < Q^2 < 6.5 \text{ GeV}^2$ .

The gas Čerenkov counter’s role was to identify inclusively scattered electrons and to reject pions during the experiment, thus providing an efficient trigger for clean electrons in a high background environment.

A description of the SANE apparatus follows in section 2. In addition to a mechanical overview, section 3 discusses the design choices and their motivation. Section 4 presents, in detail, the construction of the SANE Čerenkov counter. This is followed by a description of the detector’s calibrations and initial commissioning. Electronics and calibrations are the focus of section 4.3. Due to differences in background rates, magnetic field, and particle trajectories, the performance during each target field orientation is separately discussed in section 7. Our conclusions are described in section 8.

## 2. SANE Apparatus

To reach the statistical precision required by SANE in a limited amount of incident beam time BETA, a device unique in its open configuration, was built to provide the required angular and momentum acceptance for the experiment.

### 2.1. The BETA Detector Package

BETA comprises four detectors, a forward tracker placed as close to the target as possible, followed by a Čerenkov counter, a Lucite hodoscope and a large electromagnetic calorimeter dubbed BigCal. As can be seen in Figure 1, the front window of the Čerenkov counter was positioned just behind the forward tracker while BigCal was set at roughly 3.5m from the target. The dimensions and positions of the detectors and target are shown in Figure 2.

BigCal provided position and energy measurements of electrons and photons. It consisted of 1792 lead glass blocks and was divided into two sections. The lower section makes use of  $3.8 \text{ cm} \times 3.8 \text{ cm} \times 45 \text{ cm}$  blocks arranged in a  $32 \times 32$

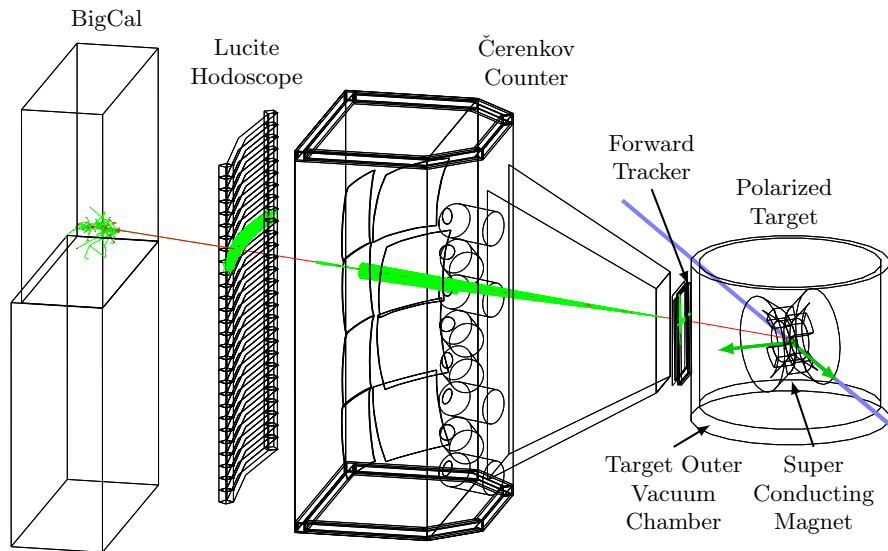


Figure 1: BETA detectors and polarized target.

grid, while the upper section contains  $4\text{ cm} \times 4\text{ cm} \times 40\text{ cm}$  blocks arranged in a  $30 \times 24$  grid.

The Lucite hodoscope includes 28 curved Lucite bars with light guides mounted to edges cut at  $45^\circ$ . Stacked vertically, each bar was 6 cm tall and 3.5 cm thick and provided a vertical position measurement. Photomultipliers (PMTs) were connected at both ends of the bar, providing an additional position determination in the horizontal direction by taking the time difference between two discriminated PMT signals.

The forward tracker used wavelength shifting fibers glued to BC-408 plastic scintillator to detect the scattered particles as close to the target as possible. Two layers of  $3\text{ mm} \times 3\text{ mm} \times 22\text{ cm}$  scintillators, stacked vertically and offset by 1.5 mm along with a layer of  $3\text{ mm} \times 3\text{ mm} \times 40\text{ cm}$  scintillators piled horizontally, provided a position measurement with a resolution sufficient to distinguish between electron and positron trajectories of momenta, below 1 GeV/c.

## 2.2. Polarized Target

Used in previous deep-inelastic scattering experiments that measured also double spin asymmetries at SLAC [2–5] and at Jefferson Lab [6], the polarized target system used a 5.1 T magnet to polarize ammonia through the mechanism of dynamic nuclear polarization. In addition to polarizing the target material, the presence of this magnetic field reduces background radiation by trapping charged particles with a momentum less than about 180 MeV. As will be discussed in section 7.2, magnetic trapping also increased background during

transverse polarization running. Due to depolarization effects, the nominal production beam current was kept roughly at about 100 nA which in turns limited the experimental luminosity to about  $\sim 1.7 \times 10^{35} \text{ cm}^{-2} \text{ s}^{-1}$  when using the 3 cm thick ammonia target.

The experiment required two target configurations, (anti-)parallel, with the magnetic field pointed along the incoming electron beam direction, and transverse, where mechanical constraints limited the target angle to be 80 degrees with respect to the beam direction. In addition to rotating the magnet, additional upstream chicane magnets were used to compensate for the beam deflection during transverse running. Deflection of background particles in the downstream target field required a non-standard beamline incorporating a helium gas bag and extended exit beam pipe.

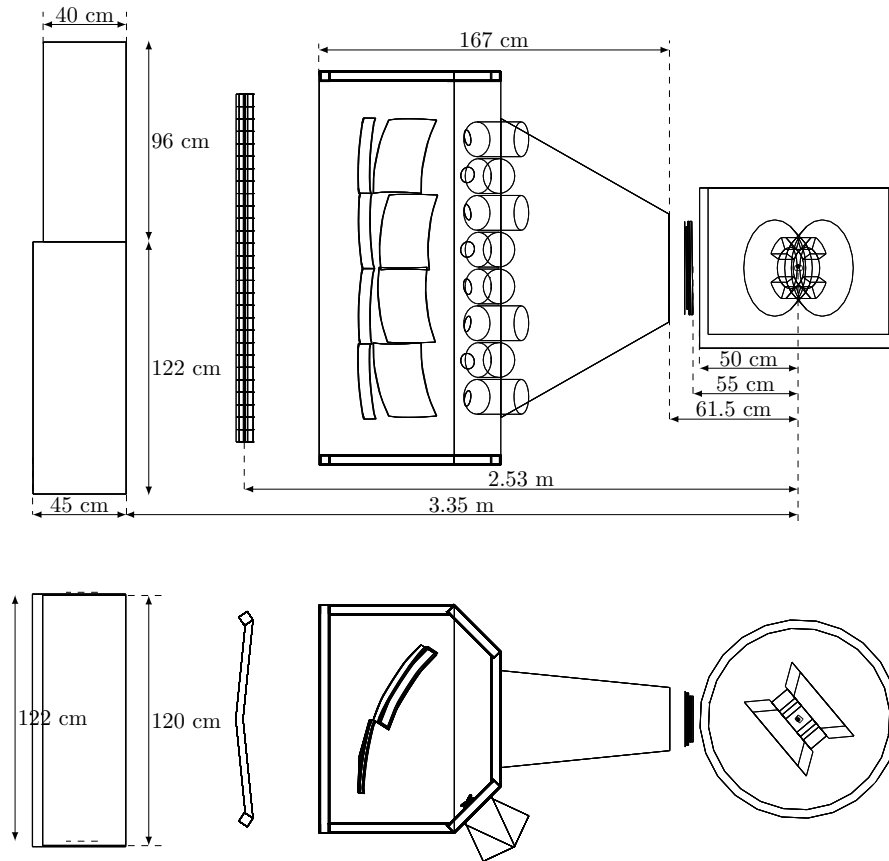


Figure 2: BETA dimensions with side view (upper figure) and a top view (lower figure). Shown from left to right are the calorimeter, hodoscope, Čerenkov counter, forward tracker and polarized target.

### 3. Design of the Čerenkov Counter

The primary requirements for the SANE gas Čerenkov counter were to identify electrons with high efficiency (greater than 90%) while maintaining a pion rejection factor better than 1000:1 with software cuts. The open configuration of the experiment required a high  $\pi^\pm$  momentum threshold to reject much of the low energy background. The Čerenkov counter needed to cover a rather large solid angle of about 200 msr and thus was placed as close as possible to the target.

Charged pions needed to be rejected for momenta up to 5 GeV. Pions above this momentum threshold should be extremely rare with a 4.7 GeV or 5.9 GeV incident electron beam and would be removed in any case with our software electron selection cuts. Looking at the thresholds for commonly used gases shown in Table 1, N<sub>2</sub> gas was selected as it best meets this rejection requirement.

<i>Charged particle</i>	N <sub>2</sub>	CO <sub>2</sub>	C <sub>4</sub> F <sub>10</sub>
$e^+, e^-$	21 MeV	17 MeV	7.8 MeV
$\mu^+, \mu^-$	4.33 GeV	3.5 GeV	1.6 GeV
$\pi^+, \pi^-$	5.75 GeV	4.6 GeV	2.1 GeV

Table 1: Čerenkov thresholds for charge particles in a N<sub>2</sub> gas at atmospheric pressure compared with other common gases.

Operating at atmospheric pressure helped simplify the mechanical design and minimize window thicknesses. The choice of a N<sub>2</sub> gas Čerenkov for radiator was a trade-off between Čerenkov photon-yield, material budget, undesired scintillation, and (ultraviolet) transparency. Although N<sub>2</sub> gas is known to scintillate, the low density and optical design minimized the impact of the isotropic scintillation background (Section 4.1). At 20°C, the index of refraction of N<sub>2</sub> gas is  $n = 1.000279$ , yielding a threshold velocity,  $\beta_0$ , for Čerenkov light emission by charged particles of

$$\beta_0 = \frac{1}{n} = 0.999721.$$

Furthermore, N<sub>2</sub> is inexpensive in comparison to other gasses making a gas recovery system unnecessary.

The leading mechanical design constraint was the optics design for focusing the Čerenkov light onto PMTs. Additional constraints on the mechanical design included a high rate of background at small angles, access to any mirrors and PMTs, and operation in the fringe magnetic field from the target.

A symmetric mirror-PMT design could not be considered as a viable option given the high background rates and long experimental run times in the area closer to the beam line. In order to allow for easy maintenance of the PMTs and to minimize worker radiation exposure[7] all PMTs were set on the large

scattering angle side of the detector. Furthermore, with the PMTs on one side (as seen in figure 2), background shielding was consolidated into two large walls.

This asymmetric design called for elliptical mirrors on the far side of the Čerenkov tank instead of spherical mirrors. Although complicating mirror procurement, these mirrors provided a focused light profile necessary to operate with three-inch diameter PMTs. Five-inch diameter tubes were initially considered, however their increased size made it very difficult to shield magnetically, and shield from background radiation. The polarized target’s 5.1 Tesla superconducting magnet sat just over one meter away necessitating a significant amount of mu-metal shielding which housed the PMTs. The mu-metal was rolled into 3 mm thick cylinders to mitigate the effects of a 100 – 200 Gauss magnetic field around the three-inch PMTs.

#### 4. Čerenkov Construction

##### 4.1. Mirror Optics

After an extensive detailed optical ray-trace analysis which included among other things the effect of the target magnetic field on the scattered electron trajectories, the shapes of the mirrors were determined[8]. The optimized result called for eight, roughly 40 cm by 40 cm glass mirrors arranged in two overlapping columns of four mirrors to cover the rather large acceptance shown in Fig 2. Four spherical mirrors cover one column at large scattering angles and four elliptical mirrors cover another column at small scattering angles. For machining purposes, the elliptical mirror was approximated with a spindle torus without any effect on the performance [9]. The dimensions of the mirrors are listed in Table 2. Light from each mirror is focussed onto individual 3-inch quartz window photomultipliers (Photonis XP4318B).

Spherical Mirror	
radius of curvature	92.0 cm
vertical size	36.5 cm
horizontal size	35.5 cm
Toroidal Mirror	
minor circle (‘tube’) radius	85.8 cm
circle of revolution (‘donut’) radius	25.8 cm
vertical size	36.5 cm
horizontal size	43.0 cm
x semiaxis (ellip. equiv.)	97.0 cm
y and z semiaxes (ellip. equiv.)	86.0 cm

Table 2: Dimensions for the spherical and toroidal mirrors. Also the torus-approximated elliptical surface’s semiaxes for a mirror in the x-y plane are given.

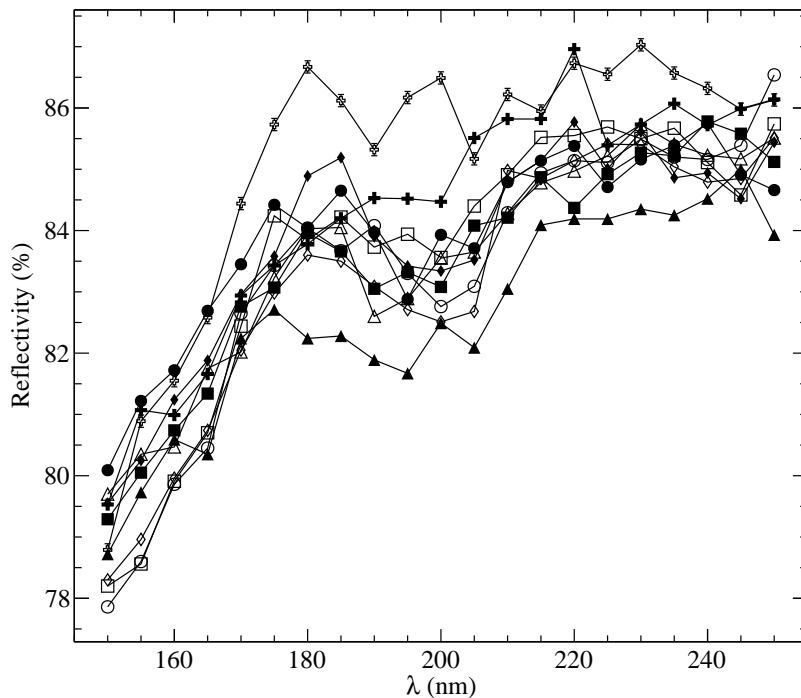


Figure 3: Mirror reflectivity as measured at CERN [10].

The glass mirrors were coated with aluminum and  $MgF_2$  for maximum reflectivity into the far UV in order to compliment the sensitivity of the photomultiplier tube at these wavelengths. The reflectivity for each mirror was measured at CERN[10] and shown in Figure 3.

The electrons of interest have momentum above 0.7 GeV/c and are deflected by the target field less than a few degrees. Thus, to a good approximation, the mirrors have been designed for point-to-point focusing from the target cell to the photomultiplier photocathodes. This permits the two towers of mirrors to be optimally aligned with a small, bright light bulb located at the same target-mirror distance. This geometry also permits good rejection of stray light from scintillation and low energy  $\delta$  rays (which are preferentially emitted at angles several times larger than the Čerenkov cone).

#### 4.2. Mirror Alignment

Mirror alignment was completed before the detector was placed into its final position. A curved u-channel assembly (Figure 4) held the mirror and connected to the frame-mounted holding arms that adjusted the mirror positions. The

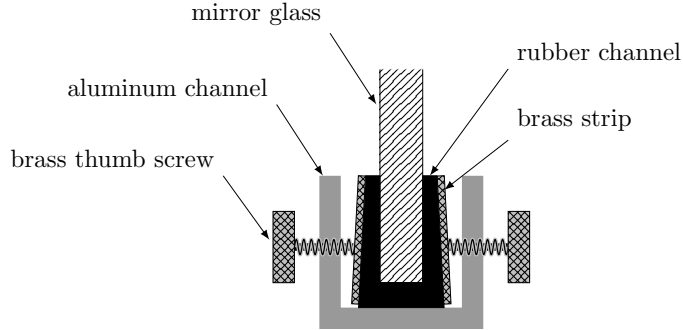
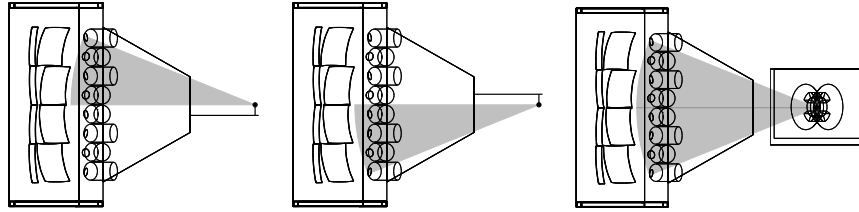


Figure 4: A cross section view of the mirror holder u-channel. The channel was machined to match the mirror curvature.

mirrors were aligned with the front window removed and using an attachment mounted to the very front of the detector, which held a small incandescent light bulb at the location of the target relative to the detector. Figures 5a and 5b show the alignment procedure using the front attachment which illuminated half of the detector at a time. A cap placed on the photo-multipliers protected them from light while the detector was open and during mirror alignment. These caps also had concentric circle targets on the outside to aid in the visual mirror alignment. With the attachment in place, the light bulb along with other tooling balls were used to survey the detector, allowing for very accurate final placement relative to the target as shown in Figure 5c.



(a) Align top mirrors. (b) Align bottom mirrors. (c) Completed mirror alignment.

Figure 5: Čerenkov mirror alignment procedure.

In order to calibrate and observe changes in the detector a LED/mirror system, shown in Figure 6, was installed inside the Čerenkov. An actuator rotated a thin mirror just inside the front window to reflect light from a LED, which also rotated to mirror the nominal target position. When not in use the mirror and LED are rotated flush against the inside of the Čerenkov snout. This LED system was used to check for position shifts after the Čerenkov was moved



into its final position near the target.

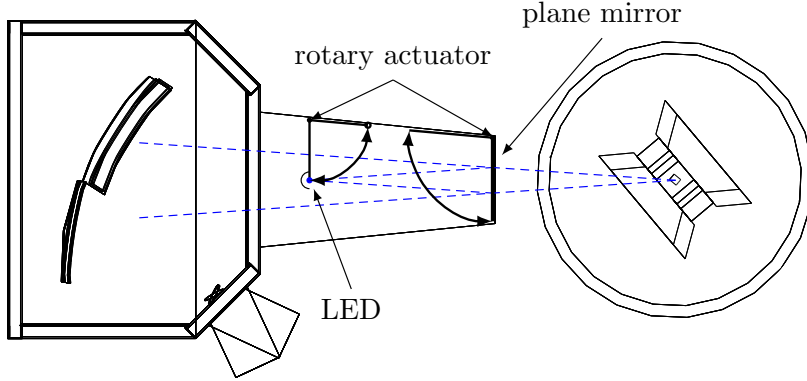


Figure 6: Plan view of the Čerenkov LED/mirror monitoring system.

#### 4.3. Photo-multipliers

Three inch diameter Photonis XP4318B quartz window photomultiplier tubes were placed inside a 3 mm thick mu-metal shield with its photocathode recessed 2 inches from the end of the cylinder as shown in Figure 7. Quartz windows provided a complementary UV transparency needed to match the reflectivity of the mirrors. Shown as the dashed-dotted curve in Figure 8, the relative efficiency of the PMT is a combination of the photo-cathode quantum efficiency, the collection efficiency and quartz window transparency. The Čerenkov photon spectrum is given by the expression

$$\frac{d^2 N}{d\lambda dx} = 2\pi\alpha\left(1 - \frac{1}{n^2\beta^2}\right)\frac{1}{\lambda^2} \quad (1)$$

where  $\alpha$  is the fine structure constant,  $\beta$  is the velocity of the particle and  $\lambda$  is the photon wavelength. The number of photons,  $N$ , is simply proportional to the gas length,  $L$ , which we take on average to be 1.3 meters.

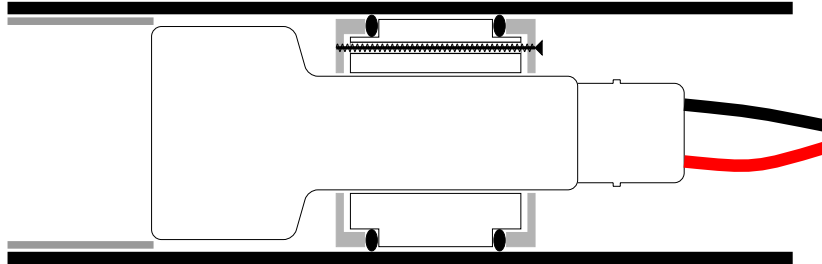


Figure 7: A diagram (not to scale) of the  $\mu$ -metal PMT holder.

Neglecting the  $N_2$  gas absorption, each scattered electron causes roughly 185 photons to fall onto the mirrors and about 155 of these reflect towards the photo-multiplier tube. From such a light pulse about 20 photo-electrons should be counted. This result can be calculated by integrating the solid curve in Figure 8 which is given by

$$\frac{dN}{d\lambda} = 2\pi\alpha\left(1 - \frac{1}{n^2\beta^2}\right)\frac{L}{\lambda^2}\eta(\lambda)R(\lambda) \quad (2)$$

where  $R$  is the reflectivity and  $\eta$  is the relative efficiency of the PMT.

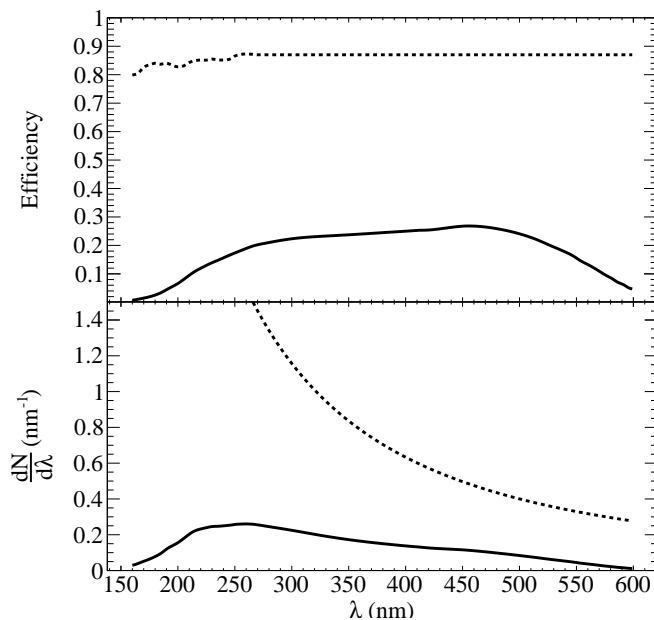


Figure 8: The mirror reflectivity (top, dashed), effective PMT quantum efficiency (top, solid line), the Čerenkov spectrum (bottom, dashed), and the photo-electron yield integrand, Eq. 2 (bottom, solid line).

#### 4.4. Gas System and Tank Construction

As previously mentioned,  $N_2$  was selected as the Čerenkov radiator gas due to the very high energy threshold for Čerenkov light production from particles heavier than an electron. Although air is mostly  $N_2$  gas, it contains moisture and other gases (such as oxygen) which attenuate and distort propagating photons.

Using a dry  $N_2$  gas source, a controller monitored and regulated the gas pressure inside the tank over the course of the experiment. A pressure transducer measured the pressure relative to the current atmospheric pressure and the controller opened and closed the appropriate solenoid valves to maintain a

differential pressure of a few torr. This slight constant overpressure reduced the possible contamination from the outside gases.

Based on initial measurements, the average delivery flow rate of gas while maintaining a differential pressure of 10 torr is less than 0.1 Standard Cubic Foot per Hour (SCFH). For an ideal hermetic and perfectly sealed Čerenkov tank this rate would be zero, and therefore this rate is also referred to as a *leak rate*. This is the rate that gas will enter the Čerenkov tank when the manometer calls for more gas and automatically opens the fill solenoid valve to maintain a set point pressure.

Flushing the tank was important once it was sealed to purge all atmospheric gas present. The controller was placed in flush mode and the relative humidity of the venting gas monitored. A relative humidity of less than a few percent was achieved in about 2 hours as shown in figure 9. Desiccant was placed at the bottom of the detector to help remove any remaining moisture from the gas.

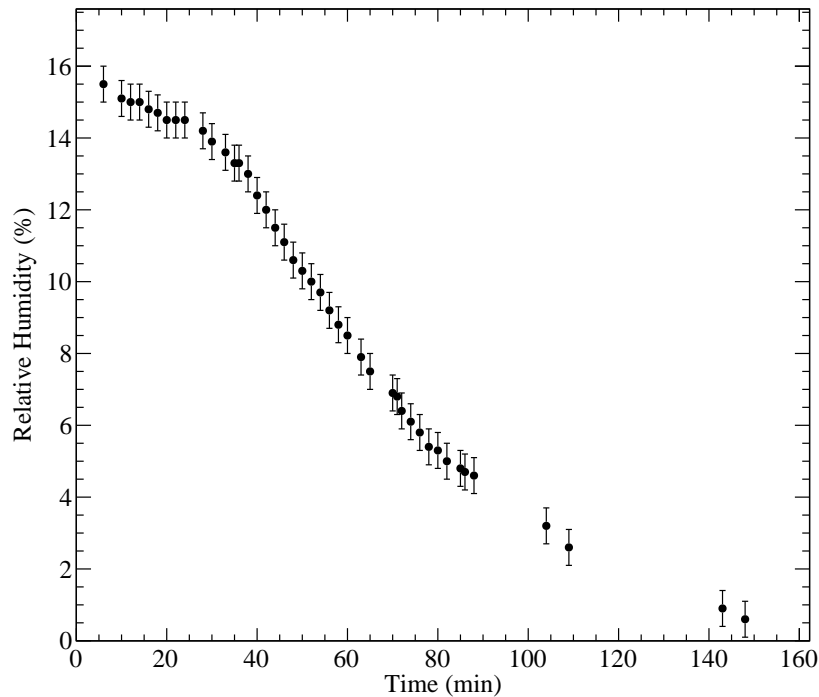


Figure 9: Relative humidity while flushing at a differential pressure of about 10 torr and a gas flow rate of 1.1 SCFM.

The tank's frame was constructed of welded and leak-checked two inch square aluminum tubing. Attached to the front of the frame was the snout which

narrows down to the front window frame holder. Attached to this frame holder was a thin piece of aluminum which is completely opaque, painted flat black, and framed by an aluminum bracket. The side panels of the main tank's frame were detachable, as was the rear window, a 1/16 inch aluminum sheet held by a large bracket. Neoprene gaskets and O-rings were used throughout when attaching or sealing any panels or flanges.

Two large lead walls were constructed to shield the PMTs from background. The first sat between the target and Čerenkov PMTs to shield them from scattering originating at the target. A second wall on the opposite side shielded the PMTs from secondary sources of scattering located around the beam dump.

## 5. Computer Simulations

A GEANT4 [11] simulation was developed to simulate the full BETA detector package called BETAG4[12]. In addition to the BETA detectors, various aspects of the experiment and apparatus were implemented such as the target geometry, materials, magnetic field and emulation of the various triggers and scalers. Beyond providing insight into the behavior of the Čerenkov counter alone, the simulation was used to explore various correlations with other detectors, observe the effects of extra material thicknesses, and study the event reconstruction from the calorimeter back to the target for each target polarization direction.

One important study undertaken using the simulation was to investigate the effect of the extra material in front of the Čerenkov counter. This extra material thickness is almost entirely due to the forward tracker (which roughly totals to the same thickness in radiation lengths as the ammonia target). Beyond the small energy loss in this material, the primary problem comes from photons, which produce electron-positron pairs in the extra material. These pairs can produce a track that is misidentified as a scattered electron by the Čerenkov counter. To understand the effects of these background events they are classified by the location of their vertex and fall in two categories.

Photons produce pairs within the target material in the central region of the target vacuum chamber, where the target magnetic field strength is quite large compared to the forward tracker location, just outside of the vacuum chamber. For these *intra-target* pairs, the strong magnetic field significantly deflects (in opposite directions) the electron and positron trajectories, so much so, that even the high energy pairs almost never produce two tracks in BETA.

However, *extra-target* pairs produced in the forward tracker material generate nearly undeflected track into BETA, and more importantly, the pair produces *twice* the amount of Čerenkov photons as a good scattered electron track. This is clearly demonstrated in the simulation results of the ADC spectrum shown in Figure 10. We will return to the discussion of the pair symmetric background in section 7.4.

## 6. Calibration and Commissioning

The PMTs were calibrated to about 100 ADC channels per photo-electron. Following a technique of photo-electron counting described in [13], the charge response of each PMT was modeled as the sum of a pedestal Gaussian, single electron response function,  $SER(x)$ , and a multiple photoelectron response  $M(x)$ . The pedestal provides the so-called “noise” function which is convoluted with the single electron response. To account for the non-ideal first dynode response and dynode noise, an exponential function is added to the ideal single (photo-) electron Gaussian function. This ideal single electron response function is defined as

$$SER_0(x) = \begin{cases} \frac{p_E}{A} e^{-\frac{x-x_p}{A}} + \frac{1-p_E}{g_N \sqrt{2\pi}\sigma_0} e^{-\left(\frac{x-x_0-x_p}{\sqrt{2}\sigma_0}\right)^2} & x > x_p \\ 0 & x < x_p \end{cases} \quad (3)$$

where  $x_p$  is the pedestal peak position,  $\sigma_p$  is the pedestal width,  $p_E$  is the fraction of events which fall under the exponential,  $A$  is the decay constant of exponential,  $x_0$  is the single photo-electron peak position, and  $\sigma_0$  is the width of the single photo-electron peak.

In order to take into account non-ideal issues such as electrical noise or ADC resolution, a noise function, defined as

$$\text{Noise}(x) = \frac{1}{\sqrt{2\pi}\sigma_p} e^{-\left(\frac{x-x_p}{\sqrt{2}\sigma_p}\right)^2}, \quad (4)$$

is convoluted with the ideal single electron response to yield a realistic single (photo-)electron response function.

$$SER(x) = (\text{Noise} \otimes SER_0)(x) \quad (5)$$

This function used in the model of the full ADC spectrum,

$$f(x) = N_0(P(0)\text{Noise}(x) + P(1)SER(x) + M(x)) \quad (6)$$

where  $P(0)$  and  $P(1)$  are the probabilities for 0 and 1 photo-electron response, and  $N_0$  is a normalization. The multiple photo-electron response,  $M(x)$  is

$$M(x) = \sum_{n=2}^{N_M} \frac{P(n; \mu)}{\sqrt{2n\pi}\sigma_1} e^{-\frac{(x-nx_1-x_p)}{2n\sigma_1^2}} \quad (7)$$

where  $\mu$  is the average number of photo-electrons,  $x_1$  ( $\simeq x_0$ ) is the average number of channels per photo-electron,  $\sigma_1$  is the average width of the (Gaussian) PMT response to a single photo-electron,  $N_M$  is the cut off in the sum which should be much greater than  $\mu$ , and  $P(n; \mu)$  is the Poisson probability distribution for  $n$  photo-electrons with mean value  $\mu$ .

In order to determine the location of the single photo-electron peak, the LED pulser was set very low,  $\mu < 0.01$ . The pedestal amplitude was roughly

determined by counting the number of events within the pedestal,  $N_p$ , and then taking the ratio to yield the zero photo-electron probability  $P(0) = N_p/N_{Tot}$ , where  $N_{Tot}$  is the total number of LED triggers.

Since  $\mu$  is much less than unity ( $\mu \ll 1$ ), the contribution of multiple photo-electrons in Eq. 6 can be neglected when fitting the LED data. An example of such a fit is shown in figure 11. Fitting yields values for the parameters  $x_p$ ,  $\sigma_p$ ,  $x_0$ , and  $\sigma_0$  for each PMT.

Next, in order to calculate the contribution from multiple photoelectrons the parameters in equation 7 are needed. To first approximation  $x_1 \simeq x_0$  and  $\sigma_1 \simeq \sigma_0$ , however, for larger signals this approximation may not hold. In order to check this, the LED pulser amplitude is turned up to  $\mu \simeq 5$ . Subsequently using the fixed parameters  $x_p$ ,  $\sigma_p$ ,  $x_0$ , and  $\sigma_0$ , a spectrum fit is performed. From this fit the values of  $\mu_1$  and  $\sigma_1$  are determined as shown in Figure 12.

For some events the Čerenkov cone is split between multiple mirrors, thus locating the mirror edges is important for knowing how to form an appropriate ADC sum. Plotting the calorimeter's cluster positions while requiring a TDC for at least two adjacent mirrors produces a projection of the mirror edges as shown in Figure 13. When a cluster falls within the region of an edge, the corresponding mirror's ADCs are added to form the Čerenkov sum associated with the cluster.

## 7. Performance

### 7.1. Data Acquisition and Analysis

The eight analog Čerenkov signals were summed using a Lecroy 428F Quad Linear Fan-In/Fan-Out NIM module. Using a single discriminator, the analog sum, in coincidence with the calorimeter, formed the primary trigger used during the SANE experiment. The performance of the SANE Gas Čerenkov is reported for two configurations which are characterized by the polarized target's magnetic field orientation.

The SANE experiment used a 5.1 Tesla superconducting magnet with its field aligned anti-parallel or transverse ( $80^\circ$ ) to the beam direction. The Čerenkov detector was exposed to very different fringe fields and background rates (Table 3) with each target field configuration. This difference in rates is primarily due to lower energy forward scattered particles circling along the polarization direction of the magnet, which in the parallel case travels along the beam direction towards the beam dump. However, for the transverse polarization, these low energy particles are directed towards the detector thus increasing the background compared to the parallel orientation. The individual PMT rates were roughly proportional to the solid angle covered by the corresponding mirror.

The detector commissioning occurred with the target polarization in the transverse orientation due to target magnet problems. Therefore, we begin by reporting the performance during the first part of the experiment.

Channel	Parallel	Perpendicular
1	33 kHz	1532 kHz
2	72 kHz	685 kHz
3	41 kHz	960 kHz
4	74 kHz	473 kHz
5	43 kHz	587 kHz
6	86 kHz	516 kHz
7	53 kHz	1023 kHz
8	60 kHz	338 kHz
Lower 4 sum	103 kHz	928 kHz
Middle 4 sum	131 kHz	1059 kHz
Upper 4 sum	114 kHz	1125 kHz
Total sum	206 kHz	1795 kHz

Table 3: Rates during normal operations for the two configurations.

### 7.2. Transverse Field Orientation

The first Čerenkov counter data were taken with the target in transverse field orientation. A few unanticipated problems arose during initial commissioning of the detector.

The spherical mirror PMTs had a slightly larger than anticipated longitudinal magnetic field component which degraded the efficiency of the PMTs on that side. Their performance degradation was monitored using the LED pulsing system. To help mitigate this inefficiency, a large 3/4-inch iron plate was quickly mounted on the front of the lead shielding wall to act as a magnetic yoke. The performance improved markedly after the plate was installed.

The transverse field production runs are characterized by high background rates on all detectors, including the Čerenkov counter. Therefore, clean event selection required a correlated calorimeter cluster and hodoscope hit. The necessity of these cuts can be seen in Figure 14. Comparing the analog sum, which was used in the trigger, to the software sum of the cluster correlated mirrors, there remained a substantial background. With the addition of a Čerenkov timing cut, the background is dramatically reduced, indicating a background composed of uncorrelated, low energy electrons or positrons, consistent with the description of nearly trapped particles in the target’s transverse magnetic field.

### 7.3. Anti-parallel Field Orientation

The background rates were significantly lower during parallel target running. Unlike the transverse configuration the software sums have much less background. Even without the aid of BETA detector event selection, the Čerenkov spectrum appeared relatively free of background as shown in Figure 16.

#### 7.4. Pair Symmetric Background Identification

It can be seen from the ADC spectra of Figures 15 and 18 that there was a significant contribution from tracks that have twice the amount of light than a single electron track produces. Most background events come from electron positron pair-production which can originate from one of two locations as previously discussed (Section 5).

Simulation has shown that *intra-target* pairs produced at the target are very unlikely to produce a double hit due to the strong (and opposite) deflections through the target magnetic field. This background cannot be removed and must be accounted for in the data analysis.

Only *extra-target* pairs remain close enough to each other to appear as a single cluster at the calorimeter. Fortunately, placing an ADC window cut on the Čerenkov ADC spectrum alone removes a significant amount of these pair events and allows for an accurate estimation of the cuts efficiency. The ADC window cut consists of the usual lower ADC limit and an upper limit located between the single and double track peaks. The precise location of the upper limit is a compromise between statistics and (extra-target) pair background rejection. For a systematic error limited measurement, pushing this limit closer to the single track eliminates a large fraction of the background, and by fitting the ADC spectrum as shown in Figure 18, the background contamination can be calculated by integrating the double track peak.

## 8. Conclusion

The SANE gas Čerenkov detector operated successfully in a high luminosity environment with an open configuration and covered a large solid angle and momentum acceptance. With a large photo-electron yield, it identified electrons with high efficiency. This large photo-electron yield provided enough ADC separation of double track events, allowing for novel event selection with the removal of (extra-target) pair symmetric background events. Although the Čerenkov counter operated efficiently under both target configurations, the transverse field orientation proved most challenging due to higher background rates.

## 9. Acknowledgements

This work is supported by DOE grant DE-FG02-94ER4084

## References

- [1] S. Choi, O. Rondon, Z.-E. Meziani, SANE Proposal (2007).
- [2] T. Averett, D. Crabb, D. Day, T. Liu, J. McCarthy, et al., A Solid polarized target for high luminosity experiments, Nucl.Instrum.Meth. A427 (1999) 440–454. doi:10.1016/S0168-9002(98)01431-4.



- [3] K. Abe, et al., Measurements of the proton and deuteron spin structure functions  $g(1)$  and  $g(2)$ , Phys.Rev. D58 (1998) 112003. [arXiv:hep-ph/9802357](#), [doi:10.1103/PhysRevD.58.112003](#).
- [4] P. Anthony, et al., Precision measurement of the proton and deuteron spin structure functions  $g(2)$  and asymmetries  $A(2)$ , Phys.Lett. B553 (2003) 18–24. [arXiv:hep-ex/0204028](#), [doi:10.1016/S0370-2693\(02\)03015-0](#).
- [5] D. McNulty, A Precise measurement of the  $G(2)$  structure function of the proton and deuteron, AIP Conf.Proc. 549 (2000) 647–650. [doi:10.1063/1.1345336](#).
- [6] F. R. Wesselmann, et al., Proton spin structure in the resonance region, Phys.Rev.Lett. 98 (2007) 132003. [arXiv:nucl-ex/0608003](#), [doi:10.1103/PhysRevLett.98.132003](#).
- [7] Jefferson lab radiation control manual (Dec 2010).  
URL <http://www.jlab.org/ehs/ehsmanual/index.html>
- [8] B. Sawatzky, Sane beta detector cherenkov mirror design tech note (staggered design), Tech. rep., Temple University (May 2005).
- [9] Eagle Glass Specialties Inc. Clarksburg, WV 26301, USA (2006).
- [10] A. Braem, Private Communication. CERN EP Division, Geneva 23 1211, Switzzeland (2007).
- [11] S. Agostinelli, et al., GEANT4: A Simulation toolkit, Nucl.Instrum.Meth. A506 (2003) 250–303. [doi:10.1016/S0168-9002\(03\)01368-8](#).
- [12] W. R. Armstrong, BETAG4 Simulation, <http://quarks.temple.edu/~whit/code/BETAG4/html/>, GEANT-4 Simulation (June 2011).
- [13] R. Dossi, A. Ianni, G. Ranucci, O. Y. Smirnov, Methods for precise photoelectron counting with photomultipliers, Nucl.Instrum.Meth. A451 (2000) 623–637. [doi:10.1016/S0168-9002\(00\)00337-5](#).

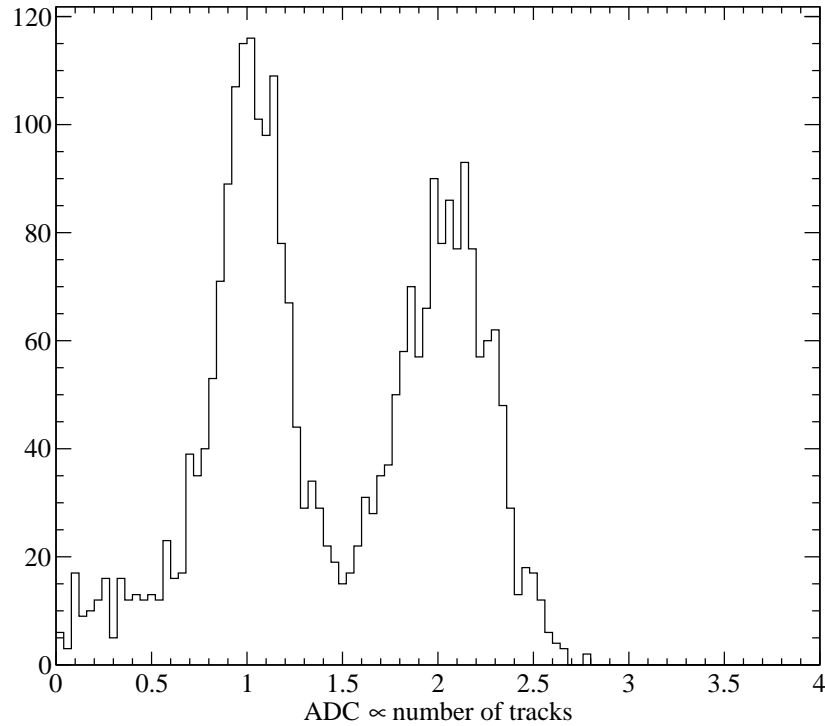


Figure 10: Simulated Čerenkov counter ADC spectrum for isotropic photons on BETA with energies uniformly sampled between 0.5 GeV and 4 GeV. The ADC values are normalized by the average ADC single for a single electron track. *Intra-target* pairs produced within the target material in the central region of the target vacuum chamber are exposed to a very strong magnetic field. This field separates the electron and positron that at least one of the particles is ejected from BETA's acceptance. *Intra-target* pairs dominate the first peak located around 1 track and *extra-target* pairs are responsible for the second (double track) peak.

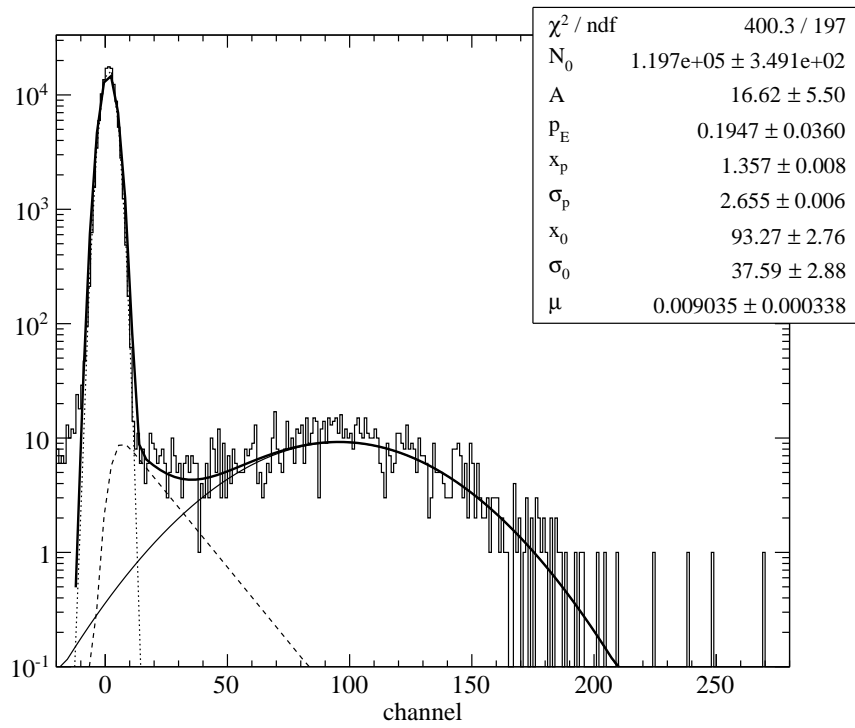


Figure 11: Single photo-electron response fit result (solid) using equation 6, neglecting the  $M(x)$  term. Also shown are the contributions from the pedestal (dotted), exponential (dashed), and Gaussian (solid) part of  $SER(x)$ .

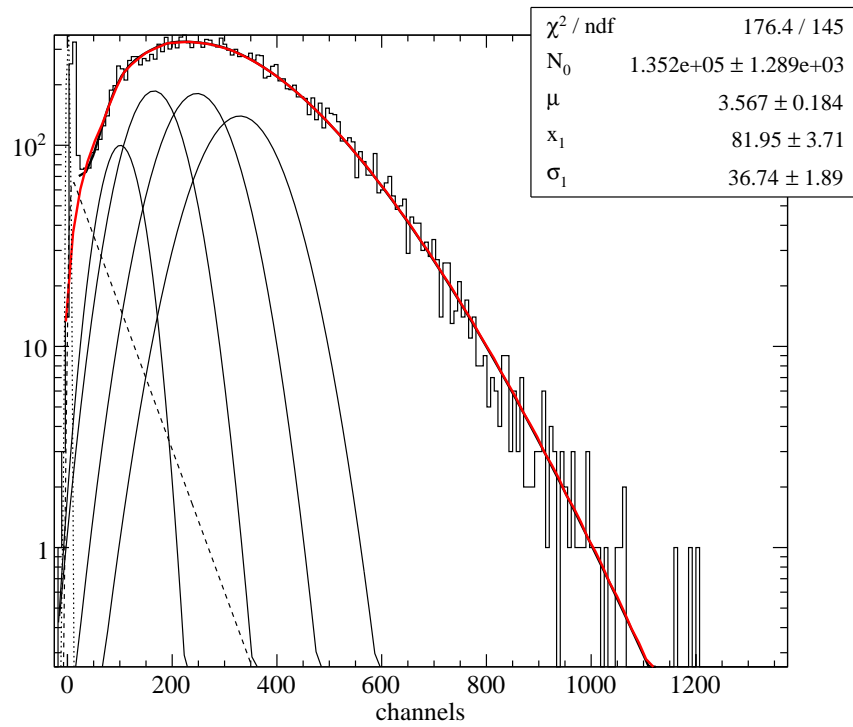


Figure 12: A fit to the photomultiplier ADC spectrum with an LED amplitude of a few photo-electrons. It shows the various terms including the pedestal (dotted), exponential (dashed), single photo-electron peak (solid), and the first few terms in the multiple photo-electron response (solid).

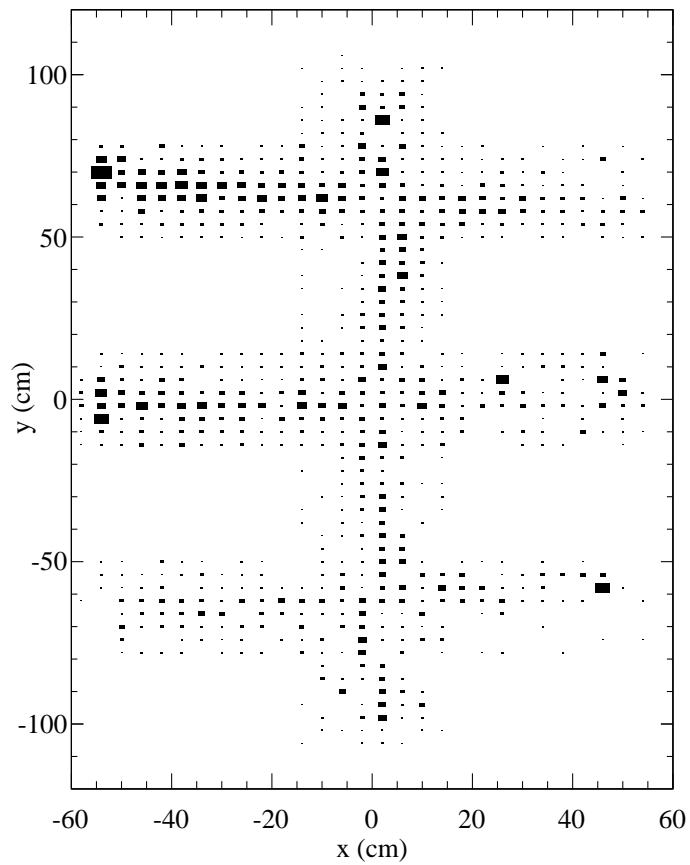


Figure 13: The mirror edges are shown in the calorimeter cluster positions when a TDC hit is required on two adjacent mirrors for a cluster. Also note how the size of the Čerenkov cone can be estimated from the distribution of events across the mirror edges.

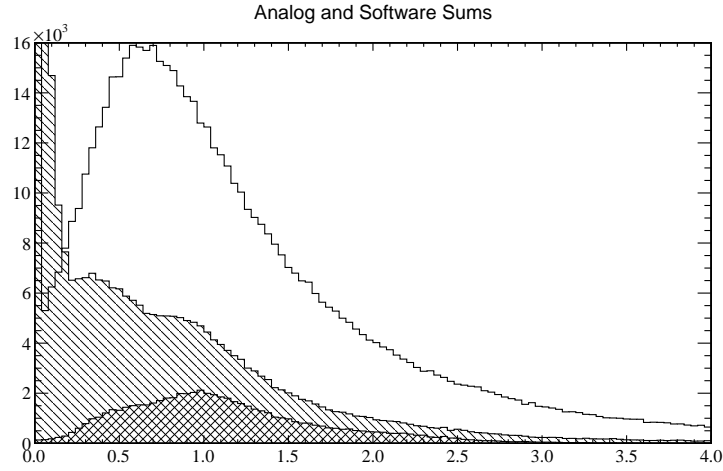


Figure 14: ADC spectra during transverse field configuration are shown: the analog sum of all eight mirrors (no hatches), cluster correlated ADC sum (single hatches), and cluster correlated ADC sum with a Čerenkov TDC cut.

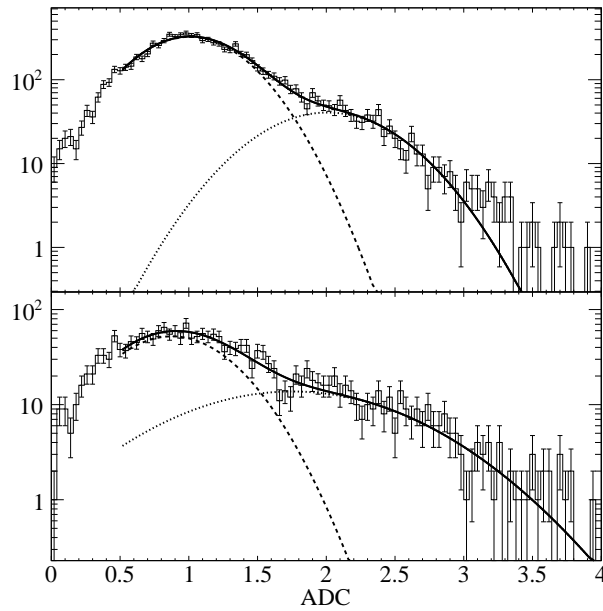


Figure 15: Čerenkov counter ADC spectrum from a transverse field configuration run for all the toroidal mirrors (top) and spherical mirrors (bottom).

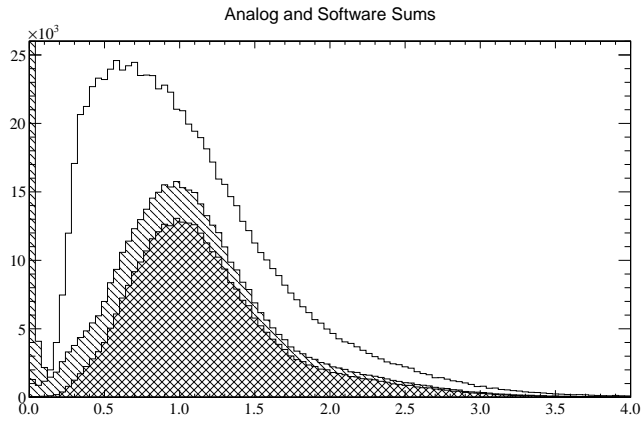


Figure 16: The histograms above show the calibrated ADC spectra for an anti-parallel configuration. The ADC spectrum of the analog sum of all eight mirrors (no hatches), cluster correlated ADC sum (single hatches), and cluster correlated ADC sum with a Čerenkov TDC cut.

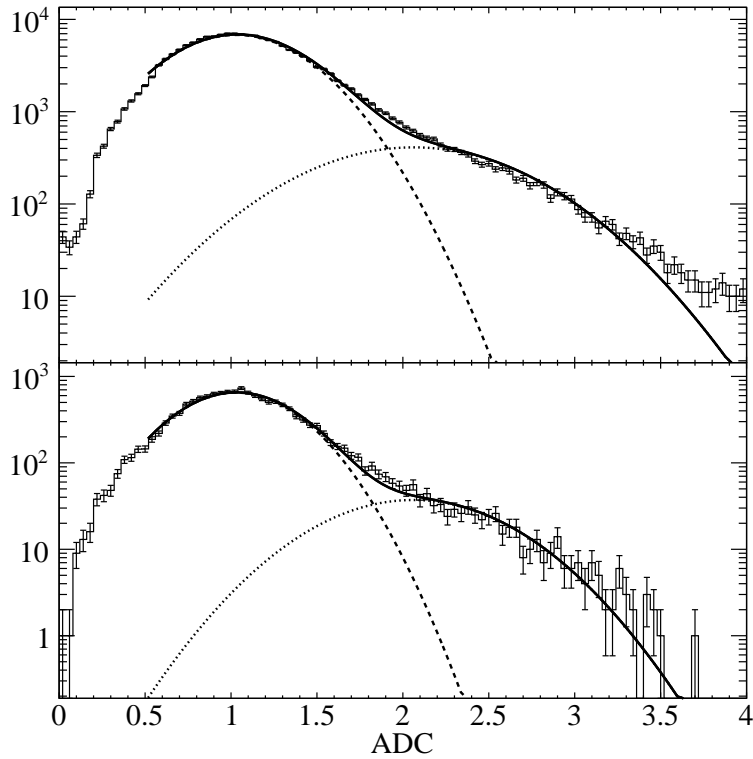


Figure 17: Same as Figure 15 for a anti-parallel field run.

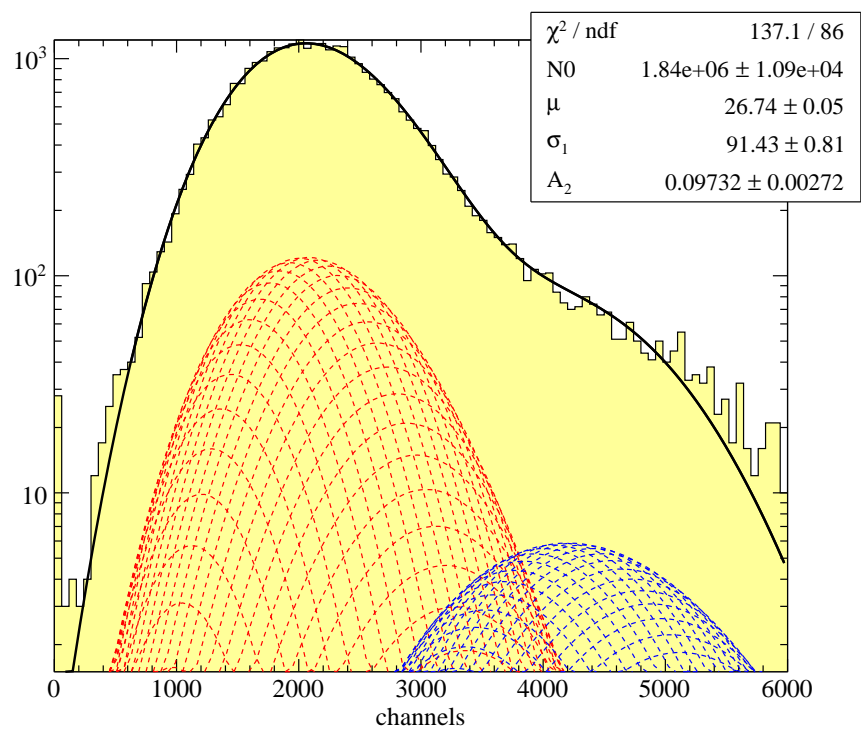


Figure 18: A typical ADC spectrum showing the one and two track peaks and the convolution fit.